



Interrelationship of bonding strength with structural stability of ternary oxide phases of MgSnO_3 : A first-principles study

B.B. Dumre, S.V. Khare*

Department of Physics and Astronomy, Wright Center for Photovoltaics Innovation and Commercialization (PVIC), University of Toledo, Toledo, OH, 43606, USA

ARTICLE INFO

Keywords:

MgSnO_3
Bonding stability
Mechanical properties
Electronic properties
Optical properties
Vibrational properties

ABSTRACT

We have studied the Ilmenite, Perovskite and LiNbO_3 type crystal structures of ternary oxide MgSnO_3 by first-principles methods using density functional theory (DFT) and beyond. We conclude that MgSnO_3 in LiNbO_3 type is both mechanically and dynamically stable, whereas Ilmenite and Perovskite crystal structures are mechanically stable but dynamically unstable. Vibrational stability in MgSnO_3 warrants some distortion in the octahedra caused due to the strength of bonding between the atom pairs Sn–O in LiNbO_3 type crystal structure. Similarly, Ilmenite and Perovskite crystal structures require a higher number of Mg–Sn and (Mg–Mg, Sn–Sn, O–O and Mg–O) bonds respectively. Ilmenite and LiNbO_3 type crystal structures can be used as window layers featuring a large bandgap of 5.22 eV and 3.88 eV respectively, along with a lower absorption coefficient and reflectivity. Likewise, Perovskite crystal structure with a bandgap of 2.55 eV can be deployed as an absorber layer that traps green light of the solar irradiation in tandem solar cells. Perovskite crystal structure has the lowest charge carrier effective masses among all the structures in MgSnO_3 . LiNbO_3 type crystal structure shows a high hardness of 56.5 GPa. It should be tested experimentally in applications requiring super-hard materials.

1. Introduction

Polycrystalline MgSnO_3 exists in three different structures, viz. LiNbO_3 type (space group $R\bar{3}c$), Ilmenite (space group $R\bar{3}$), and Perovskite (space group $Pm\bar{3}m$) crystal structures [1–7]. Recently, Fujiwara et al. [1] synthesized MgSnO_3 by molecular beam epitaxy method in the LiNbO_3 type crystal structure and measured a wide bandgap of 4.0 eV. The wide bandgap can be utilized as a prospective window layer of solar cells. Hence, MgSnO_3 in LiNbO_3 type crystal structure can be helpful in the smooth movement of charge carriers as a transparent conductive oxide layer of solar cells. Besides its experimental synthesis, some theoretical studies have also been reported. Chen et al. have utilized Modified Becke Johnson (MBJ) potential to study its opto-electronic properties [8]. Similarly, Xu et al. have studied compressive strain on it by using SCAN, MBJ and Meta Generalized Gradient Approximation (MetaGGA) potentials [9]. Likewise, study on the stability was done by Zhu et al. utilizing GGA PW91 potential with Hubbard U corrections [10].

In addition to LiNbO_3 type crystal structure of MgSnO_3 , Ilmenite crystal structure also has been experimentally synthesized by using spray pyrolysis technique at a constant substrate temperature of 350 °C

[3]. Similarly, Rani et al. also synthesized Ilmenite crystal structure using simple mixing method [4]. Likewise, Rashad et al. have also synthesized the structure in powder form using co-precipitation method [5]. Also, Kiruthiga et al. synthesized this structure using nebulizer spray pyrolysis method at a constant substrate temperature of 400 °C [2]. Various other experimental techniques have been able to prepare this structure [11–13]. No theoretical work on Ilmenite structure of MgSnO_3 has been reported yet.

Another crystal structure of MgSnO_3 is Perovskite. Experimental synthesis of this structure has not been reported yet, however, there are some theoretical works. Mahmood et al. have studied its mechanical and thermoelectric behavior using Full Potential Linearized Augmented Plane Wave (FP-LAPW) method under Perdew-Burke-Ernzerhof (PBE) GGA functional [7]. Similarly, Kumar et al. have studied the geometric prediction of its formability by studying its tolerance factor (t) defined as [6]:

$$t = r_{\text{Mg}} + r_{\text{O}} \div \sqrt{2} (r_{\text{Sn}} + r_{\text{O}}) \quad (1)$$

where r_{Mg} , r_{Sn} and r_{O} are the ionic radii of Mg, Sn and O respectively. $t = 1$ corresponds to an ideal perovskite whereas other t values represent tilting or rotation of the octahedra in the structure.

* Corresponding author.

E-mail address: sanjay.khare@utoledo.edu (S.V. Khare).

MgSnO₃ is synthesized from highly earth abundant and non-toxic metals which are relatively low cost and easily recyclable [14]. Also, their lattice constant matches with potential adjacent layer materials that helps in the experimental growth of these layers. Although these individual crystal structures are experimentally synthesized, these materials have not been utilized yet as layers in solar cells. Despite its large potential for solar energy applications, a holistic description of the various physical structures of MgSnO₃ has not been done yet. Hence, we have studied it in the three crystal structures described above, which are highly studied so far due to their relative stability over other crystal structures. Moreover, we have also computed and compared their structural, mechanical, vibrational, and opto-electronic properties. Our study reveals that some form of distortion is necessary to stabilize these structures. We have also found that Ilmenite and LiNbO₃ type crystal structures are potential window layers whereas Perovskite crystal structure can be a green light absorber layer in tandem solar cells. Additionally, LiNbO₃ type crystal structure can be utilized as a super-hard material.

2. Computational methods

All the density functional theory (DFT) and beyond computations were executed on Vienna Ab initio Simulation Package (VASP) [15–18]. The Perdew–Burke–Ernzerhof (PBE) [19,20] exchange-correlation functional was implemented in the GGA to perform the Projector-Augmented-Wave (PAW) method [21,22]. Semi-core electrons were included in the calculations in addition to the outer core. PAW PBE VASP pseudopotentials, i.e., ‘Mg_sv’, ‘Sn_d’, and ‘O_s’, were used. Plane waves of energy cut-off of 500 eV were used with a Γ -centered k-point mesh, placing 4000 k-points per reciprocal atom (KPPRA) in our calculations [23–25]. Each atom was structurally relaxed until the forces were under 0.01 eV/Å, and the convergence in energy in electronic iterations of 10⁻⁶ eV/atom was set while deploying a Gaussian smearing of width 0.05 eV [26–28]. At the beginning, initial crystal structures were taken from the Materials Project [29].

Presence of magnetic properties was also gauged during the relaxation process. After relaxation, high-precision static calculations were performed to calculate the accurate ground-state energies of the reactants and products to calculate the formation energy. Formation energy per formula unit of MgSnO₃ was calculated as [30–32]:

$$\Delta E_f = E(\text{MgSnO}_3) - E(\text{Mg}) - E(\text{Sn}) - 3E(\text{O}_2)/2 \quad (2)$$

where $E(\text{Mg})$, $E(\text{Sn})$, and $E(\text{O}_2)$ are the ground-state energies of magnesium (space group: $P6_3/mmc$), tin (space group: $I4_1/amd$), and oxygen dimer in vacuo, respectively.

Elastic constants were computed involving strained supercells by calculating the Hessian matrices of directional second derivatives of energy with respect to cell distortion using finite differences [31,33–40]. For each structure, the elastic tensor (C_{ij}) thus obtained was utilized to derive the mechanical properties following the Voigt–Reuss–Hill [26, 41–45] method, as described below:

The bulk and shear moduli in the Voigt approximation are given by:

$$B_V = [C_{11} + C_{22} + C_{33} + 2(C_{12} + C_{13} + C_{23})] / 9, \text{ and} \quad (3)$$

$$G_V = [(C_{11} + C_{22} + C_{33} - C_{12} - C_{13} - C_{23}) + 3(C_{44} + C_{55} + C_{66})] / 15 \quad (4)$$

respectively. Similarly, in the Reuss approximation, they are given by:

$$B_R = [(S_{11} + S_{22} + S_{33}) + 2(S_{12} + S_{13} + S_{23})]^{-1}, \text{ and} \quad (5)$$

$$G_R = 15 [4(S_{11} + S_{22} + S_{33} - S_{12} - S_{13} - S_{23}) + 3(S_{44} + S_{55} + S_{66})]^{-1}, \quad (6)$$

respectively, where S_{ij} is the elastic compliance tensor obtained as the inverse of elastic tensor C_{ij} . In the Hill approximation, the average bulk and shear moduli are given by:

$$B = (B_V + B_R)/2 \text{ and } G = (G_V + G_R)/2 \quad (7)$$

respectively. Eventually, Pugh’s ratio and Vickers hardness can be obtained by:

$$K = B/G \text{ and } H_V = 0.92 K^{1.137} G^{0.708} \quad (8)$$

as elaborated by Pugh [46] and Tian et al. [47–50], respectively.

Also, the mechanical stability of each structure was determined by assessing positive definiteness of elastic tensor C_{ij} as described by Born criteria [51].

Electronic bandgaps are underestimated by the GGA and the Local Density Approximation (LDA) exchange-correlation functionals [52]. Therefore, in such calculations, we implemented the Heyd–Scuseria–Ernzerhof hybrid functional (HSE06) [53,54], which combines 25% of the exact exchange from Hartree–Fock theory, and 75% of the exchange from GGA. In the context of semiconductors and insulators, this hybrid functional has been shown to predict experimental results more accurately [35,52,55,56]. Thus, by using HSE06 functional, we have calculated the electronic density of states (DOS), band structure, and frequency-dependent complex dielectric function ($\epsilon_1 + i\epsilon_2$) for all the three structures of MgSnO₃. Band structure calculation was utilized to calculate effective masses (m^*) of holes (m_h/m_0) and electrons (m_e/m_0) using the Sumo [57] package, where m_h and m_e are hole and electron masses, respectively, within the material and m_0 is the standard electron rest mass.

To gain further insight into the chemical bonding, we calculated Crystal Orbital Hamilton Populations (COHPs) using the Local-Orbital Basis Suite Towards Electric-structure Reconstruction (LOBSTER) package [32,34,48,58–64]. Furthermore, to assess the charge transferred in the formation of the compound, we calculated effective charges on each chemical species by Bader analysis [65–68]. To understand the phonon behavior inside the crystal, we used the Phonopy [69] package to calculate phonon DOS and band structure for MgSnO₃.

3. Results

3.1. Structural and energetic properties

We began our computations from three ordered conventional unit cells of the three different crystal structures, viz. Ilmenite, Perovskite and LiNbO₃ type. Conventional unit cell of Ilmenite crystal structure with space group $R\bar{3}$ has 30 atoms; where 6 atomic sites are occupied by Mg and Sn each in 6c Wyckoff positions, and 18 atomic sites are occupied by O in 18f Wyckoff positions. Also, conventional unit cell of LiNbO₃ type crystal structure with space group $R\bar{3}c$ has 30 atoms; where 6 atomic sites are occupied by Mg and Sn each in 6a Wyckoff positions, and 18 atomic sites are occupied by O in 18b Wyckoff positions. Similarly, conventional unit cell of Perovskite crystal structure with space group $Pm\bar{3}m$ has 5 atoms; where an atomic site is occupied by Mg in 1a Wyckoff position, another one atomic site is occupied by Sn in 1b Wyckoff position, and 3 atomic sites are occupied by O in 3c Wyckoff positions. Computed lattice constants for various crystal structures of MgSnO₃ are given in Table 1. Our results closely match with the earlier experimental and theoretical work [1,7,10,70]. As will be described in section 3.4, Ilmenite and LiNbO₃ type crystal structures can be beneficial window layers in solar cells. Their a-axis length has a large 6% lattice mismatch with the c-axis length of disordered-wurtzite MgSnN₂, a potential absorber layer [71,72]. Nonetheless, thin film growth may be considered in between disordered-wurtzite MgSnN₂ and Ilmenite or LiNbO₃ type MgSnO₃. This is because both the window layer Ilmenite or LiNbO₃ type MgSnO₃ and absorber layer disordered wurtzite MgSnN₂ have the same cation species, resulting in less defect formation at the interface leading to better charge collection and efficiency.

No magnetic moments were found in any of the three structures investigated. All the three crystal structures have the same octahedral

Table 1

Lattice constants, in Å, of MgSnO_3 in the three different crystal structures, along with their formation energies per atom, in eV, calculated using the GGA functional. Values from the literature are listed where available.

Crystal Structure		Lattice Constants (Å)			Formation Energy (eV)
Name	Space Group	a	b	c	
Ilmenite	$R\bar{3}$	5.26,	=	13.90,	-4.02
		5.2342 ^a	a	13.8690 ^a	
Perovskite	$Pm\bar{3}m$	4.02, 4.00 ^b	=	= a	-3.59
			a		
LiNbO ₃ type	$R3c$	5.30,	=	14.17,	-4.22
		5.211 ^c ,	a	14.24 ^c ,	
		5.29 ^d		14.18 ^d	

^a Experimental Ref. [12,70].

^b Theoretical Ref. [7].

^c Experimental Ref. [1].

^d Theoretical Ref. [9,10].

atomic arrangements with coordination number six. Perovskite crystal structure has regular octahedra with all the $\angle\text{OMO}$ being right angles, where M is either magnesium or tin, formed between any two adjacent oxygen atoms. However, there is distortion in the octahedra of Ilmenite and LiNbO₃ type crystal structures as shown in Fig. 1, referred to as Jahn-Teller distortions [73]. This can be attributed to the cubic crystal with higher symmetry in the Perovskite crystal structure against the rhombohedral crystal with lower symmetry in the other two crystal structures. The distortion can be understood by the average bond lengths of first nearest neighbors between Mg–O and Sn–O within each crystal structure as given in Supplementary Table S1. The Mg–O distances in Ilmenite and LiNbO₃ type crystal structures are lesser than in Perovskite, whereas Sn–O distances in Ilmenite is lesser and LiNbO₃ type is higher than in Perovskite, thereby causing the distortion. As will be discussed in sections 3.3 and 3.4 below, LiNbO₃ type crystal structure is relatively stable than the other two, where the distances in Mg–O (2.05 Å) is smaller than the distances in Sn–O (2.06 Å). In contrast, Ilmenite and Perovskite have Mg–O (2.11 Å and 2.84 Å) distances larger than Sn–O (1.89 Å and 2.01 Å) distances. Thus, there seems to have an association between the Mg–O distances being lower than Sn–O distances and relative stability in these three ternary oxides.

The formation energies, from Eq. (2), of all the three structures are also given in Table 1. The LiNbO₃ type crystal structure has the lowest formation energy per atom making it more stable than the other two phases. Thus, LiNbO₃ type crystal structure is the global minimum in the formation energy for MgSnO_3 consistent with earlier theoretical work [74]. As will be discussed in sections 3.2 and 3.3 below, the other crystal

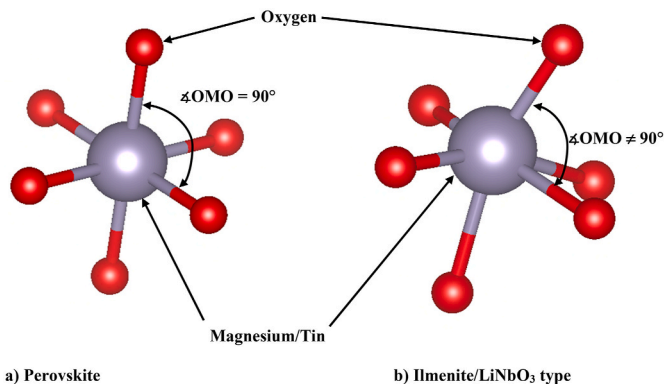


Fig. 1. Octahedra formed by six oxygen atoms (red) and one central either magnesium or tin atom (grey) in a) Perovskite crystal structure and b) Ilmenite or LiNbO₃ type crystal structure. Figure was created using VESTA software [97]. (For interpretation of the references to color in this figure legend, the reader is referred to the Web version of this article.)

structures are mechanically stable but vibrationally unstable, which is also consistent with the calculated values of formation energy being higher for them.

3.2. Mechanical properties

Values of elastic and mechanical properties such as elastic constants, mechanical stability, bulk modulus, shear modulus, Pugh's ratio, and Vickers hardness for the respective crystal structures of MgSnO_3 , are given in Supplementary Tables S2 to S4. Due to the different crystal symmetries of each phase of MgSnO_3 , direct comparison of all elastic constants is not possible. However, elastic constant C_{11} , related to axial compression, is higher in the Perovskite structure than the other two which have comparable values. Similarly, elastic constant C_{12} , related to dilation on compression, is higher in the Ilmenite structure than the other two, out of which LiNbO₃ type has the higher value than the Perovskite. Similarly, the elastic constant C_{44} , related to shear deformations, is higher in LiNbO₃ type crystal structure than the other two, where the other two have similar values. The bulk and shear moduli in the three phases decrease in the order: LiNbO₃ type > Perovskite > Ilmenite. This puts LiNbO₃ type crystal structure more resilient to both bulk and shear deformations. According to Born criteria [51], all the three crystal structures are mechanically stable. The Pugh's ratio in the three phases decrease in the order: Ilmenite (2.98) > Perovskite (2.22) > LiNbO₃ type (1.82). As the high value of Pugh's ratio is indicative of malleability/ductility and low value of brittleness, Ilmenite crystal structure is more malleable/ductile, and LiNbO₃ type crystal structure is more brittle out of these three phases. The Vickers hardness decrease in the order: LiNbO₃ type (56.5 GPa) > Perovskite (39.5 GPa) > Ilmenite (22.2 GPa). These hardness values are higher than that of well-known solar cell materials such as Si (11.77 GPa) [75] and CdTe (0.49 GPa) [76]. Hence, MgSnO_3 in all these phases will be mechanically suitable for application in solar cell layers. Besides solar usage, these materials are one of the hardest materials comparable to others used in hard-coatings industry such as TiN (25 GPa), ZrC (27 GPa), HfN (20 GPa), TaC (26 GPa), etc [77–80]. LiNbO₃ type phase should be investigated further experimentally as a potential super-hard material.

3.3. Vibrational properties

Fig. 2 displays the band structure and DOS of phonons for all the three crystal structures. For LiNbO₃ type crystal structure, we do not observe any phonon frequency below zero, which makes it dynamically stable out of these three crystal phases. Both Perovskite and Ilmenite are dynamically unstable. To be experimentally grown on a substrate, the crystal structure needs to be both mechanically and dynamically stable. In this connection, there has been no experimental study on Perovskite crystal structure. However, Ilmenite crystal structures have been grown by using spray pyrolysis method at a constant substrate temperature of 350 °C [3]. As our DFT calculations have been done at 0 K, these phonons may behave differently at higher temperatures due to their mutual interaction and the structure could become stable [35]. Similarly, Perovskite crystal structure also might be experimentally viable. As Ilmenite crystal structure has phonon population up to – 4 THz and Perovskite crystal structure up to – 10 THz, Perovskite crystal might need higher temperature for its crystal growth.

Further, we can observe that O gives rise to prominent peaks in the higher frequency range around 15 THz, the Mg peaks around 10 THz, and the Sn peaks around 5 THz in all phases. This determines that the lighter particles have higher vibrational frequencies than the heavier ones. In Perovskite and Ilmenite crystal structures, a gap is observed in the phonon bands of value 3.01 THz and 8.47 THz around frequency level of 15 THz and 20 THz respectively, whereas there is no such gap in LiNbO₃ type crystal structure. These phonon gaps help Ilmenite and Perovskite crystal structures to be used as sound filters and mirrors as any phonon of frequency within the gap will not traverse in the material

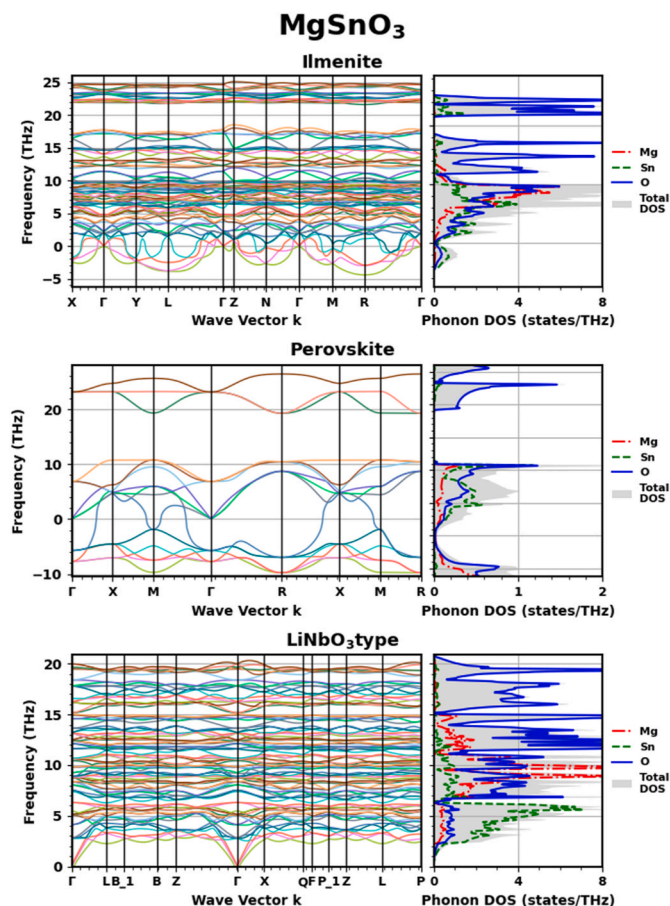


Fig. 2. Comparison of the phonon band structures and densities of states (DOS) per unit cell of MgSnO_3 for different crystal structures, computed using the GGA functional.

and thus will be reflected from the surface [81].

3.4. Electronic properties

Supplementary Figure S1 shows the electronic DOS for each structure of MgSnO_3 computed using the hybrid HSE06 functional. The Fermi level in all the three phases is closer to the valence band, hence, they are all p-type materials. O and Sn states dominate around the Fermi level in all the three crystal phases, except for the conduction band of Perovskite type structure where Mg states are also prominent. Supplementary Figure S2 displays Sn DOS separated into the t_{2g} and e_g states for each structure of MgSnO_3 computed using the hybrid HSE06 functional. For octahedral coordination, the e_g states must be above the t_{2g} states according to the Crystal Field Theory (CFT) [82,83], and such behavior is observed in all the crystal phases. Perovskite crystal structure has a higher value of the e_g states at a significantly higher energy level above the t_{2g} , but the same is not true for other two crystal structures. In Ilmenite and LiNbO_3 type phases, the e_g states are in slightly higher energy level above the t_{2g} states and the t_{2g} states have a bigger peak compared to the e_g ones. This directly corresponds to the distortion in the octahedra of Ilmenite and LiNbO_3 type phases compared to the regular octahedra of Perovskite phase. We conclude that some distortion is necessary in the octahedra for the stability of MgSnO_3 [84] because LiNbO_3 type phase is stable, as discussed in the previous paragraph. Moreover, Ilmenite crystal structure is also found stable experimentally at a higher temperature. In addition to this, Ilmenite crystal structure also has a lower negative value of its phonon frequency than the Perovskite structure. Whenever the octahedra is distorted, the metal atoms come more closer than in the regular octahedra which helps to

form metallic bonds as the apices of the e_g orbitals will interact and cause the t_{2g} states to rise up in the energy level and occupy more states [85]. The design of stabilization due to the strength of such metallic bonds help to stabilize the LiNbO_3 type and Ilmenite crystal structures. To elaborate these findings, Supplementary Figure S3 shows bonding interaction between atomic orbitals projected from the plane waves known as pCOHP computed using GGA functional [19,20]. It is a dimensionless quantity, and its negative value means positive bonding, positive value means anti-bonding, and zero is non-bonding. As shown in Supplementary Figure S3, all the nearest neighbor interactions above the Fermi level in the conduction band are in anti-bonding states as electronic states are loosely bound there. Interaction between Mg–O does not have any substantial anti-bonding states below the Fermi level for all the three phases. However, Sn–O and O–O interactions have anti-bonding states below the Fermi level in all the phases but in varying quantity. Clearly, the most unstable Perovskite crystal has larger number of anti-bonding states than the other two. It has anti-bonding states of Sn–O interaction above around -3 eV, whereas O–O interactions above around -1.5 eV. Similarly, the total number of anti-bonding states in Ilmenite crystal structure is in between the other two structures. It has anti-bonding states of both Sn–O and O–O interactions starting above around -3 eV with substantial states above around -1 eV. Finally, LiNbO_3 type crystal structure has the least number of anti-bonding states where both Sn–O and O–O interactions have anti-bonding states arising above around -1 eV. Besides the three interactions shown in the figure, other metal-metal interactions are not shown because they are about a tenth in relative strength, compared to others. However, they can be valuable to understand the origin of instability in the structure. Hence, $2 \times 2 \times 2$ supercell calculations were performed in order to encompass all the atomic interactions. Thus, we have computed and analyzed the integrated result of pCOHP from -10 eV to the Fermi level known as IpCOHP. Its dimension is equivalent to that of energy and its larger value suggests larger bonding strength and vice-versa. Supplementary Table S5 displays the values of IpCOHP in all the three crystal phases for the interactions between all the pairs of metal-metal (Mg–Mg, Mg–Sn and Sn–Sn), metal-oxygen (Mg–O, Sn–O) and oxygen-oxygen (O–O). Sn–O and total interactions have IpCOHP value increasing in the order: Perovskite < Ilmenite < LiNbO_3 type. Specifically, Sn–O interaction helps in stabilizing LiNbO_3 type crystal structure. Mg–O interaction has just the opposite trend to what just discussed for the earlier interactions and helps to stabilize Perovskite structure. Also, the interactions of same atomic species (Mg–Mg, O–O and Sn–Sn) help to stabilize Perovskite structure as they have higher value of IpCOHP in Perovskite structure than the other two. Similarly, the Mg–Sn interaction has a lower value of IpCOHP for Ilmenite crystal structure and helps to stabilize it. If interactions between Mg–Mg, O–O, Sn–Sn, and Mg–O become stronger by phonon interaction or other means at high temperature, the possibility of stabilizing Perovskite structure exist whereas strengthening Mg–Sn bonds may stabilize Ilmenite structure. To strengthen a particular kind of bond, theoretically we can also think of intentionally substituting the metal atoms in the octahedra in such a way as we maximize the number of a particular kind of bond. In doing so, the local octet rule may be violated, and bandgaps may change as well. To quantify the changes when such disorder is applied, further study on the topic is necessary [86].

To understand the degree of ionicity or covalency of the bonds existing between cation and anion, we computed effective charges on these atoms as the charge transferred from cation to anion. Supplementary Table S6 displays the charges transferred from Mg to O and Sn to O in all the three phases of MgSnO_3 calculated using the GGA functional. There is not much variation in the charge transferred from Mg to O in contrast to the charge transferred from Sn to O. This can be attributed to the spherical s-orbital of Mg in the valence state while compared to the various apices of d-orbitals and its splitting in Sn. As all the charges transferred are more than $1e$, the bonds are ionic and the ionicity is higher in the bonds between Sn–O rather than Mg–O. The

electronegativities of Mg, Sn and O are 1.23 e , 1.72 e and 3.50 e respectively, based on electrostatic force calculated by Allred et al. [87]. Although the difference between electronegativities of atoms in Mg–O bonds (2.27 e) is higher than in Sn–O bonds (1.78 e), we surmise that the higher charge-transferred from Sn to O compared to Mg to O can be attributed to the higher number of valence electrons of 4 in Sn while compared to 2 in Mg.

Bandgaps for all the three crystal structures of MgSnO₃ calculated using the hybrid HSE06 functional are given in Table 2. All the bandgaps are indirect in nature. Bandgap for Ilmenite crystal structure is 5.22 eV where the electronic transition takes place from k-point (−0.333, 0.167, 0.000) to $\Gamma(0, 0, 0)$. Likewise, the bandgap for Perovskite phase is 2.55 eV with transitions taking place from k-point R(0.5, 0.5, 0.5) to $\Gamma(0, 0, 0)$. Similarly, the bandgap for LiNbO₃ type crystal structure is 3.88 eV that transits electron from k-point (0.167, 0.167, 0.000) to $\Gamma(0, 0, 0)$. Experimentally reported bandgap of 4.0 eV for LiNbO₃ type crystal phase closely matches with our result. For other two crystal phases, experimental bandgap has not been reported yet and our results are predictions for future experimental work. Fig. 3 displays the band structure for Perovskite crystal structure that clearly displays the transitions that takes place between the valence band maximum (VBM) and the conduction band minimum (CBM). The band structures of other two phases are not shown due to the high computing resources required. The bandgaps of Ilmenite and LiNbO₃ type crystal structures are higher than the energy (3.26 eV) of violet color in the visible range. Beyond that energy, Air Mass 1.5 Global (AM 1.5 G) solar irradiation (shown in Fig. 4) also does not have substantial power to produce electron-hole pair. Hence, Ilmenite and LiNbO₃ type crystal structures can be used as window layers in solar cells. Similarly, the Perovskite crystal structure can be used as a green light absorber in the tandem solar cells.

Bond lengths can be beneficial to describe the variation in bandgap in different crystal structures with the same atomic constituents. Longer bonds produce smaller bandgaps and vice versa in strained materials [88]. From Table S1, average of the bond lengths in the three phases of MgSnO₃ increase in the order: Ilmenite > LiNbO₃ type > Perovskite consistent with their bandgaps, shown in Table 2.

Table 2 provides both electron and hole effective masses in all the three crystal phases of MgSnO₃. VBM and CBM curvatures were taken while calculating the effective masses. Both hole and electron effective masses increase in the order: Perovskite < Ilmenite < LiNbO₃ type. We observed earlier that Ilmenite and LiNbO₃ type crystal structures can be utilized as window layers. As Ilmenite crystal structure has lower effective masses than LiNbO₃ type crystal structure, Ilmenite crystal structure can be a better candidate for charge carrier transportation in the window layer. The effective masses of Perovskite (0.33), Ilmenite (0.60) and LiNbO₃ type (0.71) crystal structures are lower than that of silicon (1.06) [89], making them good candidates as absorber and

Table 2

Bandgaps, in eV, and effective masses, in standard electron rest mass m_0 , of MgSnO₃ in the three different crystal structures calculated using the hybrid HSE06 functional. Bandgaps calculated using the GGA functional are also given for comparison. Values from the literature are listed where available.

Crystal Structure		Bandgap (eV)		Effective Mass (m^*)	
Name	Space Group	GGA	HSE06	Electron (m_e^*)	Hole (m_h^*)
Ilmenite	$R\bar{3}$	3.42; indirect	5.22; indirect	0.60	45.42
Perovskite	$Pm\bar{3}m$	0.88; indirect	2.55; indirect	0.33	1.97
LiNbO ₃ type	$R3c$	2.26; indirect, 2.8 ^a	3.88; indirect, 4.0 ^b , 3.61; indirect ^c	0.71	112.28

^a Theoretical (GGA + U) Ref. [10].

^b Experimental Ref. [1].

^c Theoretical (MBJ) Ref. [9].

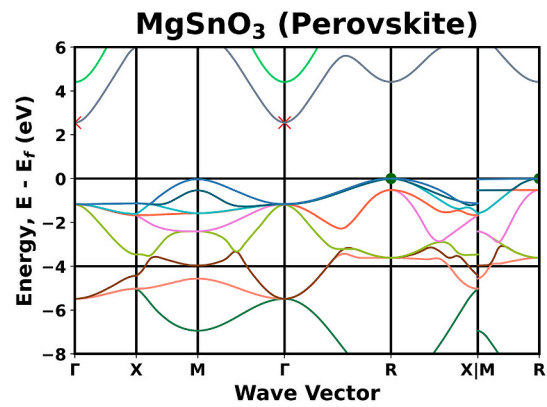


Fig. 3. Electronic band-structure diagrams of energy vs. wave vector for MgSnO₃ for Perovskite crystal structure, computed using the hybrid HSE06 functional. Red crosses represent the conduction band minima; green dots represent the valence band maxima. Fermi energy (E_f) is set at 0 eV. (For interpretation of the references to color in this figure legend, the reader is referred to the Web version of this article.)

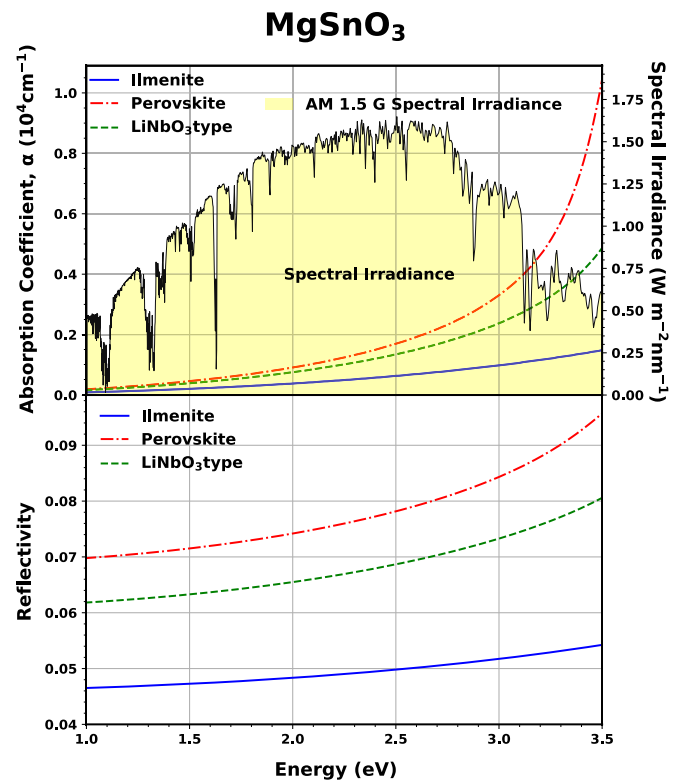


Fig. 4. Absorption coefficient, α (top panel), and reflectivity (bottom panel) curves, left axis, of MgSnO₃ for the three different crystal structures computed using the hybrid HSE06 functional. Standard AM 1.5 G solar spectral irradiance [94], right axis, is illustrated in the yellow shaded area along with the absorption curve. (For interpretation of the references to color in this figure legend, the reader is referred to the Web version of this article.)

window layers in new types of solar cells with alternative materials. However, the mobility in Perovskite crystal structure can be lesser than in silicon as there is a possibility of higher alloy scattering [90]. In all the crystal phases, electron effective masses are lower than hole effective masses. For Perovskite crystal structure, it can be observed from Fig. 3 that the higher dispersion in the conduction band than in the valence band leads to lower effective masses in electrons. Therefore, electron effective masses are 6 times lighter than hole effective masses in

Perovskite crystal structures.

3.5. Optical properties

Ilmenite and LiNbO₃ type crystal structure are anisotropic in their interactions with photons in parallel (||) and perpendicular (⊥) directions with respect to *ab* plane as shown in Figure S4. Perovskite crystal structure is isotropic due to its cubic symmetry. Complex dielectric function data for photon energies 0–10 eV is provided in Supplementary Tables S7 and S8. The dielectric constants of Perovskite (2.92), Ilmenite (2.29) and LiNbO₃ type (2.66) crystal structures are lower than that of Si (11.7) [91], where the average of two directions is considered for Ilmenite and LiNbO₃ type crystal structures. The dielectric constants for the three phases of MgSnO₃ are nearly the same. It is harder to achieve a higher efficiency due to these lower dielectric constants because the probability of charge separation is reduced due to weakly screened coulombic attraction [92].

The complex dielectric functions for Ilmenite, Perovskite, and LiNbO₃ type crystal structures are plotted in Figures S5, S6 and S7, respectively. Real part shows the first peak around the bandgap of each material in each direction for all the three phases of MgSnO₃. Similarly, some positive value in imaginary part is observed for each material after the bandgap. For the anisotropic crystal phases, both the real and imaginary parts have overall similar character over the range of photon energies displayed in the figures. Right after the first peaks in the real part of the dielectric function in all the crystal phases, the other peaks decline except in the parallel direction of Ilmenite crystal structure. Similarly, the imaginary part increases after the first peak in all the crystal structures. In all the crystal phases of MgSnO₃, above around 15 eV of photon energy, the real part starts to increase and the imaginary part decreases. The peaks in the real and imaginary parts of the dielectric function in all the phases denote various inter- and intra-band transitions [93]. For the visible range, 1.63 eV–3.26 eV, real parts in all the phases nearly plateau around their dielectric constant whereas the imaginary parts plateau at zero.

Fig. 4 shows plots of absorption coefficient and reflectivity versus photon energy for all the three crystal structures of MgSnO₃, where average of all the directions was considered for Ilmenite and LiNbO₃ type crystal structures. The spectral irradiance of the AM 1.5 G spectrum [94] is also plotted along with the absorption coefficient for comparison. There is not significant absorption in any of the three crystal structures in the visible region, because the absorption coefficient resulting in substantial efficiency in solar cells must be around 10⁵ cm⁻¹ [95], and these materials have only below 10⁴ cm⁻¹. However, the absorption slowly rises for the higher photon energy for all the crystal phases. The rise in the absorption coefficient is higher in Perovskite crystal structure which is beneficial as it can be utilized as an absorber layer. Out of the other two crystal phases, Ilmenite crystal structure has lower absorption coefficient rise which is beneficial as a window layer in solar cells. The reflectivity is near to zero for all the crystal structures. Behavior of the reflectivity curves is equivalent to the absorption curves. Such a lower reflection makes Perovskite phase a better absorber, whereas the other two phases a better window layer.

4. Conclusion

We have computationally studied the structural, mechanical, vibrational, and opto-electronic properties of MgSnO₃ in the three different crystal forms. Our study confirms that MgSnO₃ in LiNbO₃ type is both mechanically and dynamically stable, whereas Ilmenite and Perovskite crystal structures are mechanically stable but dynamically unstable. The underlying reason behind the vibrational stability has been understood as the distortion in octahedra caused due to the strength of bonding between Sn–O atoms in LiNbO₃ type crystal structure. In order to stabilize Ilmenite and Perovskite crystal structures, future endeavors must be carried towards increasing the number of Mg–Sn and (Mg–Mg, Sn–Sn,

O–O and Mg–O) bonds respectively. Bandgap, absorption coefficient and reflectivity suggest that Ilmenite and LiNbO₃ type crystal structures can be used as window layers, whereas Perovskite crystal structure can be utilized as an absorber layer that captures green light of the solar irradiation in a tandem solar cell. Our study on the charge carrier effective masses has confirmed that Perovskite crystal structure has the lowest effective masses among all the structures in MgSnO₃, whereas Ilmenite crystal structure has lower effective masses than LiNbO₃ type crystal structure to be used as a window layer. Beyond solar cell usage, LiNbO₃ type crystal structure with Vickers hardness of 56.5 GPa can be utilized as a super-hard material.

Disclaimer

The views and conclusions contained herein are those of the authors and should not be interpreted as necessarily representing the official policies or endorsements, either expressed or implied, of Air Force Research Laboratory or the U.S. Government.

Declaration of competing interest

The authors declare that they have no known competing financial interests or personal relationships that could have appeared to influence the work reported in this paper.

Acknowledgement

We thank the Ohio Supercomputer Center (OSC) [96] for computational resources. This material is based on research sponsored by Air Force Research Laboratory under agreement number FA9453-18-2-0037. We also thank The National Science Foundation Division of Civil, Mechanical, and Manufacturing Innovation through grant 1629239. The U.S. Government is authorized to reproduce and distribute reprints for Governmental purposes notwithstanding any copyright notation thereon.

Appendix A. Supplementary data

Supplementary data to this article can be found online at <https://doi.org/10.1016/j.physb.2022.413896>.

References

- [1] K. Fujiwara, et al., *Thin-film stabilization of LiNbO₃-type ZnSnO₃ and MgSnO₃ by molecular-beam epitaxy*, *Apl. Mater.* 7 (2) (2019) 22505.
- [2] G. Kiruthiga, et al., *DSSCs: a facile and low-cost MgSnO₃-based transparent conductive oxides via nebulized spray pyrolysis technique*, *J. Mater. Sci. Mater. Electron.* 32 (18) (2021) 22780–22791.
- [3] G.K. Prabhu, C. Sanjeeviraja, *Structural, optical, Electrical and Hall effect studies of Spray pyrolysed MgSnO₃ Thin films*, *International Journal of ChemTech Research* 6 (3) (2014) 1942–1944.
- [4] E. Rani, et al., *Investigation on physical and optical properties of the SnO₂-MgO nanocomposite at different compositions mixings*, *Jurnal Teknologi* 78 (5) (2016).
- [5] M.M. Rashad, H. El-Shall, *Effect of synthesis conditions on the preparation of MgSnO₃ powder via co-precipitation method*, *Powder Technol.* 183 (2) (2008) 161–168.
- [6] A. Kumar, A.S. Verma, S.R. Bhardwaj, *Prediction of formability in perovskite-type oxides*, *Open Appl. Phys. J.* 1 (1) (2008) 11–19.
- [7] Q. Mahmood, et al., *The study of mechanical and thermoelectric behavior of MgXO₃ (X = Si, Ge, Sn) for energy applications by DFT*, *Chem. Phys.* 524 (2019) 106–112.
- [8] X.-Y. Chen, et al., *First-principles study of R₃C-MgSnX₃ (X=O, S and Se) for photovoltaic and ferroelectric application*, *Phys. Lett.* 422 (2022) 127774.
- [9] X.-F. Xu, et al., *Tuning mechanical properties, ferroelectric properties and electronic structure in R₃C-MgSnO₃ by compressive strain: a first-principle study*, *Physica B: Phys. Condens. Matter* 618 (2021) 413143.
- [10] W.-L. Zhu, et al., *Theoretical study of stability and electronic structure of the new type of ferroelectric materials XSnO₃ (X= Mn, Zn, Fe, Mg)*, *Int. J. Mod. Phys. B* 28 (31) (2014) 1450224.
- [11] C.S. Lim, *A facile solvothermal Process to synthesize MSnO₃ (M= Sr, Mg) nanoparticles Assisted by microwave irradiation*, *Asian J. Chem.* 25 (6) (2013) 3211–3214.
- [12] X. Liu, *Synthesis, phase structure and dielectric property of the ZnO–MgO–SnO₂ ceramics*, *J. Alloys Compd.* 558 (2013) 131–135.

- [13] A.V. Loginov, et al., Synthesis of oxide materials in the Mg–Sn–O system for use in composite solid electrolytes, *Russ. J. Appl. Chem.* 90 (3) (2017) 496–498.
- [14] F. Kawamura, et al., *Synthesis of a novel rocksalt-type ternary nitride semiconductor MgSnN₂ Using the metathesis reaction under high pressure*, *Eur. J. Inorg. Chem.* 2020 (5) (2020) 446–451.
- [15] G. Kresse, J. Furthmuller, Efficiency of ab-initio total energy calculations for metals and semiconductors using a plane-wave basis set, *Comput. Mater. Sci.* 6 (1) (1996) 15–50.
- [16] G. Kresse, J. Furthmuller, Efficient iterative schemes for ab initio total-energy calculations using a plane-wave basis set, *Phys. Rev. B* 54 (16) (1996) 11169–11186.
- [17] G. Kresse, J. Hafner, Ab initio molecular dynamics for liquid metals, *Phys. Rev. B* 47 (1) (1993) 558–561.
- [18] G. Kresse, J. Hafner, Ab initio molecular-dynamics simulation of the liquid-metal–amorphous-semiconductor transition in germanium, *Phys. Rev. B* 49 (20) (1994) 14251–14269.
- [19] J.P. Perdew, et al., Erratum: atoms, molecules, solids, and surfaces: applications of the generalized gradient approximation for exchange and correlation, *Phys. Rev. B* 48 (7) (1993) 4978.
- [20] J.P. Perdew, et al., Atoms, molecules, solids, and surfaces: applications of the generalized gradient approximation for exchange and correlation, *Phys. Rev. B* 46 (11) (1992) 6671–6687.
- [21] P.E. Blochl, Projector augmented-wave method, *Phys. Rev. B* 50 (24) (1994) 17953–17979.
- [22] G. Kresse, D. Joubert, From ultrasoft pseudopotentials to the projector augmented-wave method, *Phys. Rev. B* 59 (3) (1999) 1758–1775.
- [23] S.V. Khare, T.L. Einstein, N.C. Bartelt, Dynamics of step doubling: simulations for a simple model and comparison with experiment, *Surf. Sci.* 339 (3) (1995) 353–362.
- [24] A.W. Ghosh, S.V. Khare, Rotation in an asymmetric multidimensional periodic potential due to colored noise, *Phys. Rev. Lett.* 84 (23) (2000) 5243.
- [25] J.L. Roehl, et al., Binding sites and diffusion barriers of a Ga adatom on the GaAs (001)-c(4X4) surface from first-principles computations, *Phys. Rev. B* 82 (16) (2010).
- [26] P.P. Gunaicha, et al., *Structural, energetic and elastic properties of Cu₂ZnSn(S_xSe_{1-x})₄ (x = 1, 0.75, 0.5, 0.25, 0) alloys from first-principles computations*, *Sol. Energy* 102 (2014) 276–281.
- [27] N. Jiang, et al., *An ab initio computational study of pure Zn₃N₂ and its native point defects and dopants Cu, Ag and Au*, *Thin Solid Films* 564 (2014) 331–338.
- [28] Y.J. Wang, et al., Thermal equation of state of silicon carbide, *Appl. Phys. Lett.* 108 (6) (2016) 5.
- [29] A. Jain, et al., Commentary: the Materials Project: a materials genome approach to accelerating materials innovation, *Apl. Mater.* 1 (1) (2013) 11.
- [30] I.S. Khare, et al., Electronic, optical, and thermoelectric properties of sodium pnictogen chalcogenides: a first principles study, *Comput. Mater. Sci.* 183 (2020) 109818.
- [31] V. Adhikari, et al., *First-principles study of mechanical and magnetic properties of transition metal (M) nitrides in the cubic M₄N structure*, *J. Phys. Chem. Solid.* 120 (2018) 197–206.
- [32] N.J. Szymanski, et al., *Prediction of improved magnetization and stability in Fe_{1-x}N₂ through alloying*, *J. Appl. Phys.* 126 (9) (2019) 93903.
- [33] X. Wu, D. Vanderbilt, D.R. Hamann, Systematic treatment of displacements, strains, and electric fields in density-functional perturbation theory, *Phys. Rev. B* 72 (3) (2005) 35105.
- [34] V. Adhikari, et al., First principles investigation into the phase stability and enhanced hardness of TiN–ScN and TiN–YN alloys, *Thin Solid Films* 688 (2019) 137284.
- [35] N.J. Szymanski, et al., Dynamical stabilization in delafossite nitrides for solar energy conversion, *J. Mater. Chem.* 6 (42) (2018) 20852–20860.
- [36] K. Balasubramanian, S.V. Khare, D. Gall, Energetics of point defects in rocksalt structure transition metal nitrides: thermodynamic reasons for deviations from stoichiometry, *Acta Mater.* 159 (2018) 77–88.
- [37] Z. Liu, et al., First-principles phase diagram calculations for the rocksalt-structure quaternary systems TiN–ZrN, TiN–HfN and ZrN–HfN, *J. Phys. Condens. Matter* 29 (3) (2016) 35401.
- [38] K. Balasubramanian, S. Khare, D. Gall, Vacancy-induced mechanical stabilization of cubic tungsten nitride, *Phys. Rev. B* 94 (17) (2016) 174111.
- [39] K. Zhang, et al., Growth and mechanical properties of epitaxial NbN(001) films on MgO(001), *Surf. Coating. Technol.* 288 (2016) 105–114.
- [40] K. Zhang, et al., *Epitaxial NbC_xN_{1-x}(001) layers: growth, mechanical properties, and electrical resistivity*, *Surf. Coating. Technol.* 277 (2015) 136–143.
- [41] G. Grimvall, in: E. Wohlfarth (Ed.), *Thermophysical Properties Of Materials, Ser. Selected Topics in Solid State Physics*, North-Holland, Amsterdam, 1986, p. 18.
- [42] R. Hill, The elastic behaviour of a crystalline aggregate, *Proc. Phys. Soc.* 65 (5) (1952) 349–354.
- [43] A. Reuss, Berechnung der fließgrenze von mischkristallen auf grund der plastizitätsbedingung für einkristalle, *ZAMM-Journal of Applied Mathematics and Mechanics/Zeitschrift für Angewandte Mathematik und Mechanik* 9 (1) (1929) 49–58.
- [44] X. Zhou, D. Gall, S.V. Khare, *Mechanical properties and electronic structure of anti-ReO₃ structured cubic nitrides, M₃N, of d block transition metals M: an ab initio study*, *J. Alloys Compd.* 595 (2014) 80–86.
- [45] W. Voigt, *Lehrbuch der kristallphysik*, vol. 962, Teubner Leipzig, 1928.
- [46] S.F. Pugh, Xcii. Relations between the elastic moduli and the plastic properties of polycrystalline pure metals, *Londn. Edinburgh Dublin Philos. Mag. J. Sci.* 45 (367) (1954) 823–843.
- [47] Y. Tian, B. Xu, Z. Zhao, Microscopic theory of hardness and design of novel superhard crystals, *Int. J. Refract. Metals Hard Mater.* 33 (2012) 93–106.
- [48] Z.T.Y. Liu, D. Gall, S.V. Khare, Electronic and bonding analysis of hardness in pyrite-type transition-metal pernitrides, *Phys. Rev. B* 90 (13) (2014) 134102.
- [49] Z.T.Y. Liu, et al., First-principles investigation of the structural, mechanical and electronic properties of the NbO-structured 3d, 4d and 5d transition metal nitrides, *Comput. Mater. Sci.* 84 (2014) 365–373.
- [50] Z.T.Y. Liu, et al., Structural, mechanical and electronic properties of 3d transition metal nitrides in cubic zincblende, rocksalt and cesium chloride structures: a first-principles investigation, *J. Phys. Condens. Matter* 26 (2) (2014) 25404.
- [51] M. Born, On the stability of crystal lattices. I, *Math. Proc. Camb. Phil. Soc.* 36 (2) (1940) 160–172.
- [52] J. Paier, et al., Screened hybrid density functionals applied to solids, *J. Chem. Phys.* 124 (15) (2006) 154709.
- [53] J. Heyd, G.E. Scuseria, M. Ernzerhof, Hybrid functionals based on a screened Coulomb potential, *J. Chem. Phys.* 118 (21) (2003) 8207–8215.
- [54] A.V. Kruckau, et al., Influence of the exchange screening parameter on the performance of screened hybrid functionals, *J. Chem. Phys.* 125 (22) (2006) 224106.
- [55] N.J. Szymanski, et al., Electronic and optical properties of vanadium oxides from first principles, *Comput. Mater. Sci.* 146 (2018) 310–318.
- [56] Z.T.Y. Liu, et al., *Transparency enhancement for SrVO₃ by SrTiO₃ mixing: a first-principles study*, *Comput. Mater. Sci.* 144 (2018) 139–146.
- [57] A.M. Ganose, A.J. Jackson, D.O. Scanlon, sumo: command-line tools for plotting and analysis of periodic ab initio calculations, *J. Open Source Softw.* 3 (28) (2018) 717.
- [58] V.L. Deringer, A.L. Tchougreff, R. Dronskowski, Crystal orbital Hamilton population (COHP) analysis as projected from plane-wave basis sets, *J. Phys. Chem.* 115 (21) (2011) 5461–5466.
- [59] R. Dronskowski, P.E. Blochl, Crystal Orbital Hamilton Populations (COHP). Energy-resolved visualization of chemical bonding in solids based on density-functional calculations, *J. Phys. Chem.* 97 (33) (1993) 8617–8624.
- [60] S. Maintz, et al., Analytic projection from plane-wave and PAW wavefunctions and application to chemical-bonding analysis in solids, *J. Comput. Chem.* 34 (29) (2013) 2557–2567.
- [61] S. Maintz, et al., LOBSTER: a tool to extract chemical bonding from plane-wave based DFT, *J. Comput. Chem.* 37 (11) (2016) 1030–1035.
- [62] S. Maintz, M. Esser, R. Dronskowski, Efficient rotation of local basis functions using real spherical harmonics, *Acta Phys. Pol. B* 47 (4) (2016) 1165–1175.
- [63] N.J. Szymanski, et al., Unconventional superconductivity in 3d rocksalt transition metal carbides, *J. Mater. Chem. C* 7 (40) (2019) 12619–12632.
- [64] Z.T.Y. Liu, et al., First-principles phase diagram calculations for the rocksalt-structure quaternary systems TiN–ZrN, TiN–HfN and ZrN–HfN, *J. Phys. Condens. Matter* 29 (3) (2017) 35401.
- [65] G. Henkelman, A. Arnaldsson, H. Jónsson, A fast and robust algorithm for Bader decomposition of charge density, *Comput. Mater. Sci.* 36 (3) (2006) 354–360.
- [66] E. Sanville, et al., Improved grid-based algorithm for bader charge allocation, *J. Comput. Chem.* 28 (5) (2007) 899–908.
- [67] W. Tang, E. Sanville, G. Henkelman, A grid-based Bader analysis algorithm without lattice bias, *J. Phys. Condens. Matter* 21 (8) (2009) 84204.
- [68] M. Yu, D.R. Trinkle, Accurate and efficient algorithm for Bader charge integration, *J. Chem. Phys.* 134 (6) (2011) 64111.
- [69] A. Togo, I. Tanaka, First principles phonon calculations in materials science, *Scripta Mater.* 108 (2015) 1–5.
- [70] JCPDS PDF No: 00-030-0798, 1980.
- [71] B.B. Dumre, D. Gall, S.V. Khare, *Stability, and electronic and optical properties of ternary nitride phases of MgSnN₂: a first-principles study*, *J. Phys. Chem. Solid.* 153 (2021) 110011.
- [72] N. Yamada, et al., *Band gap-tunable (Mg, Zn)SnN₂ earth-abundant Alloys with a wurzite structure*, *ACS Appl. Electron. Mater.* 3 (11) (2021) 4934–4942.
- [73] H.A. Jahn, E. Teller, F.G. Donnan, Stability of polyatomic molecules in degenerate electronic states, *Proc. Roy. Soc. Londn. Ser. A Math. Phys. Sci.* 161 (905) (1937) 220–235.
- [74] S.G. Kang, First-principles examination of low tolerance factor perovskites, *Int. J. Quant. Chem.* 117 (19) (2017) e25420.
- [75] J.P. Zanatta, et al., Growth of HgCdTe and CdTe(331)B on germanium substrate by molecular beam epitaxy, *Appl. Phys. Lett.* 71 (20) (1997) 2984–2986.
- [76] S. Cole, M. Brown, A.F.W. Willoughby, *The microhardness of Cd_xHg_{1-x}Te*, *J. Mater. Sci.* 17 (7) (1982) 2061–2066.
- [77] K. Balasubramanian, S.V. Khare, D. Gall, Valence electron concentration as an indicator for mechanical properties in rocksalt structure nitrides, carbides and carbonitrides, *Acta Mater.* 152 (2018) 175–185.
- [78] B.D. Ozsdolay, et al., *Cubic β-WN₂ layers: Growth and properties vs N-to-W ratio*, *Surf. Coating. Technol.* 304 (2016) 98–107.
- [79] S. Kodambaka, et al., Absolute orientation-dependent anisotropic TiN(111) island step energies and stiffnesses from shape fluctuation analyses, *Phys. Rev. B* 67 (3) (2003) 35409.
- [80] J. Barenó, et al., Orientation-dependent mobilities from analyses of two-dimensional TiN (111) island decay kinetics, *Thin Solid Films* 510 (1–2) (2006) 339–345.
- [81] R.M. Hornreich, et al., Phonon band gaps, *J. Phys.* 7 (3) (1997) 509–519.
- [82] J.H. Van Vleck, Theory of the variations in paramagnetic anisotropy among different salts of the iron group, *Phys. Rev.* 41 (2) (1932) 208–215.
- [83] H. Bethe, Termaufspaltung in Kristallen, *Ann. Phys.* 395 (2) (1929) 133–208.
- [84] R.H. Mitchell, *Perovskites: Modern and Ancient*, vol. 7, Almaz Press Thunder Bay, 2002.

- [85] I. Khatri, et al., Correlating structure and orbital occupation with the stability and mechanical properties of 3d transition metal carbides, *J. Alloys Compd.* 891 (2022) 161866.
- [86] D. Han, et al., *Cation disorder in stoichiometric MgSnN₂ and ambipolar self-doping behavior in off-stoichiometric MgSnN₂*, arXiv (2021) arXiv:2110.14289.
- [87] A.L. Allred, E.G. Rochow, A scale of electronegativity based on electrostatic force, *J. Inorg. Nucl. Chem.* 5 (4) (1958) 264–268.
- [88] N. Tit, I.M. Obaidat, H. Alawadhi, Origins of bandgap bowing in compound-semiconductor common-cation ternary alloys, *J. Phys. Condens. Matter* 21 (7) (2009) 75802.
- [89] M.A. Green, Intrinsic concentration, effective densities of states, and effective mass in silicon, *J. Appl. Phys.* 67 (6) (1990) 2944–2954.
- [90] B.E. Warren, B.L. Averbach, B.W. Roberts, Atomic size effect in the X-ray scattering by alloys, *J. Appl. Phys.* 22 (12) (1951) 1493–1496.
- [91] C. Kittel, *Introduction to Solid State Physics*, John Wiley&Sons., New York, 2005.
- [92] K.J.T. Hamam, *Organic Solar Cells Based on High Dielectric Constant Materials: an Approach to Increase Efficiency*, in Department of Physics, Western Michigan University: Graduate College at ScholarWorks at Western Michigan University, 2013, p. 107.
- [93] R. Deng, et al., Optical and transport measurement and first-principles determination of the ScN band gap, *Phys. Rev. B* 91 (4) (2015) 45104.
- [94] N.R.E. Laboratory, *Reference Air Mass 1.5 Spectra*, 2003. Available from: <https://www.nrel.gov/grid/solar-resource/spectra-am1.5.html>.
- [95] B.B. Dumre, et al., *Improved optoelectronic properties in CdSe_xTe_{1-x} through controlled composition and short-range order*, *Sol. Energy* 194 (2019) 742–750. Ohio Supercomputer Center, 1987.
- [96] K. Momma, F. Izumi, VESTA 3 for three-dimensional visualization of crystal, volumetric and morphology data, *J. Appl. Crystallogr.* 44 (6) (2011) 1272–1276.